Large-eddy simulation of oxygen transfer to organic sediment beds

Carlo Scalo,[1] Ugo Piomelli,[1] and Leon Boegman[2]

[1]   We have developed a model for dissolved oxygen (DO) transfer from water to underlying organic sediment beds. The model couples large-eddy simulation (LES) of turbulent transport in the water column, a biogeochemical model for DO transport and consumption in the sediment, and Darcy's Law for the pore water-driven transport. The model highlights the spatial and temporal relationship between the turbulent bursting events, the near-wall transport of DO, and the response of the sediment layer. The numerical results—compared to data from laboratory experiments—stress the importance of analyzing instantaneous transport events (not reproducible in a Reynolds-averaged Navier-Stokes model) to better characterize and model the processes that lead to oxygen depletion in the sediment layer. The model's results are compared against experimental data and the sensitivity to the governing parameters has been tested. As the current velocity increases, the sediment-oxygen demand (SOD) increases more slowly than the friction velocity at the wall, in accordance with classic heat-and-mass transfer laws. The overall SOD is approximately proportional to the bacterial content of the sediment layer. The predicted mean advective flux in the porous medium and across the sediment-water interface is negligible compared to the total dispersive flux, for permeabilities typical of the sediments used in the experiments (10^{-7} and 10^{-6} cm^2). Higher permeabilities (10^{-5} cm^2) appear to yield results not consistent with experimental data. This computational tool will contribute toward the design of a process-oriented parametrization for the SOD, currently missing in oceanographic applications, that can be easily extended to the transport of other bio-limiting substances.

1. Introduction

[2] The presence of dissolved oxygen (DO) in water is critical to the survival of organisms in marine environments. Surface waters are saturated with atmospheric oxygen, which is transported toward the bottom by turbulent motions. A number of physical factors can limit this mixing process. For instance, stratification in the water column damps turbulence, reducing mixing; this inhibits the vertical DO flux, reducing the oxygen supply to deeper unstratified water layers. Other factors of biogeochemical nature may amplify this problem, such as agricultural runoff containing excess nutrients, which fertilize algal blooms. This process can lead to a severe alteration of the natural ecosystem balance in coastal regions (on which a significant portion of the world population relies for their sustenance). The algae eventually die and sink to the bed; in the sediment layer, DO-consuming bacteria feed on them. When the DO flux to the sediments (and biological demand) is greater than the flux through the stratified layer near-bed oxygen depletion can occur. The amount of DO absorbed by the sediment will, as a result, largely govern the oxygen budget in such bottom water layers [*Bouldin*, 1968; *Veenstra and Nolen*, 1991; *Patterson et al.*, 1985]; if the lack of oxygen persists, aquatic life may suffer. Areas affected by this phenomenon are known as 'dead zones', and can be found in many coastal environments in the ocean (the Gulf of Mexico, Chesapeake Bay, the Baltic sea or the Black Sea) or even in lakes (Lake Erie). Further details on the spreading of dead zones in the coastal oceans and their effect on marine ecosystems can be found in *Diaz and Rosenberg* [2008] and *Rabalais et al.* [2010].

[3] Because of the environmental and economical consequences of oxygen depletion, there has been significant effort to understand the processes governing DO transport through the water column and the sediment-water interface and ultimately DO depletion by bacterial absorption in the sediment layer. Being able to model these mechanisms is a necessary step toward the development of prediction tools to improve water-management strategies. Research in this field

[1]Department of Mechanical and Materials Engineering, Queen's University, Kingston, Ontario, Canada.
[2]Department of Civil Engineering, Queen's University, Kingston, Ontario, Canada.

Corresponding author: C. Scalo, Department of Mechanical and Materials Engineering, Queen's University, McLaughlin Hall, 130 Stuart St., Kingston, ON K7L 3N6, Canada. (cscalo.ca@gmail.com)

has been carried out mainly through laboratory and field experiments, and numerical investigations limited to one- or two-dimensional models.

[4] Perhaps the first study of this kind is due to *Lorke et al.* [2003], who measured and analyzed turbulence induced by oscillatory fluid motions and vertical distribution of DO above and within the sediments in Lake Alpnach (Switzerland). Their analysis focuses on the near-sediment region, and shows how the intensity of the turbulent transport controls the thickness of the diffusive sublayer, and the diffusive DO flux across the sediment-water interface (SWI). An extension of this work can be found in *Bryant et al.* [2010] where the transient nature of the sediment oxygen uptake is examined, as well as the importance of characterizing turbulence when correlating it to the oxygen flux to the sediments. This is the first attempt to link sediment oxygen demand (SOD) directly to large-scale dynamics such as oscillatory currents, extending the knowledge of how physical processes can be used to model SOD, taking into account the features of non-equilibrium flows.

[5] The same problem has also been investigated experimentally. *Hondzo et al.* [2005] performed DO laboratory measurements in a closed loop recirculating square duct. The oxygen dissolved in the water was absorbed by a synthetically generated sediment layer containing organic compost. They derived a scaling law for the mean DO profiles in water, for Reynolds numbers between 360 and 4000 (based on the half-width of the flume and centreline mean velocity). Using the same experimental setup, *O'Connor and Hondzo* [2007] analyzed DO depletion mechanisms in the sediment layer. More recently, *O'Connor and Hondzo* [2008] obtained complete DO measurements (in water and sediments) together with PIV characterization of the turbulent flow in order to correlate the transfer rate of oxygen to the sediments with the Reynolds and Schmidt numbers of the flow. These set of experiments have been chosen as a reference for our numerical study. Their results are compared with semi-empirical solute transport models in turbulent flows [*Boudreau and Jørgensen*, 2001]. The experiments show a marked dependence of the DO at the sediment-water interface (SWI) and of the SOD on the turbulent activity in the flow.

[6] The first attempt, to our knowledge, to design a numerical and physical model to reproduce experimental observations such as the ones by Hondzo and co-workers was made by *Higashino et al.* [2004], who adopted an unsteady DO diffusion and absorption model coupled with a one-dimensional solution of the Reynolds-Averaged equations for the water-side transport. The biochemical model used for oxygen diffusion and absorption by the sediment layer includes a non-linear sink term and a diffusion term. An extension of this work can be found in *Higashino et al.* [2008] who performed a simulation of a developing boundary layer, using the algebraic eddy-viscosity model of *Dade* [1993] to parameterize turbulent transport, coupled with an improved version of the DO sediment absorption model. The new formulation takes into account the biomass concentration of oxygen-consuming bacteria, χ^*, in the sediment layer. Although, in principle, $\chi^* = \chi^*(t)$, this quantity remains nearly constant over typical experimental timescales, and a steady state value of χ^* was calibrated to match experimental data. However, their numerical model does not

reproduce the observed DO profiles at higher Reynolds numbers; this lack of agreement was attributed to the absence of a model for pore water flow induced transport of DO in the sediment layer.

[7] The influence of pore water flow on solute transport across the SWI was investigated by *Higashino et al.* [2009] using an approximate characterization of the turbulent pressure oscillations driving the flow in the sediments according to Darcy's Law. The interstitial flow was used to predict solute advection across the SWI and effective diffusivity (primarily dispersion) in the sediment layer, D_e (proportional to the intensity of the pore water flow and sediment grain size). Their model resulted in an underestimation of D_e with respect to the empirically based parametrization of *O'Connor and Harvey* [2008]. Also, the model was not explicitly coupled with a water-side or sediment-side scalar-transport model, so an analysis of the effects of turbulence-driven pore water flow on solute transport was not possible. The highest permeability investigated resulted in a fluctuation intensity of the surface-normal component of the oscillating interstitial velocity of 0.02% of the friction velocity. More recently, *Higashino and Stefan* [2011] extended the effective diffusivity parametrization of *Higashino et al.* [2009] and incorporated it into the same RANS model of *Higashino et al.* [2008] predicting an increase in the sediment oxygen uptake with the sediment permeability. However, the change they obtain in the dissolved oxygen distribution—increased penetration depth and decreased concentration value at the SWI—increases the disagreement between the numerical predictions and the experimental data at higher Reynolds numbers.

[8] Although the existence of a direct dependency of the SOD on the turbulence levels has been extensively demonstrated (but not fully understood), in most water-quality models used for lake and ocean management, the SOD is simply a tuneable parameter, fixed in time (and often space), and chosen over an order of magnitude scale so that DO observations can be reproduced. These models typically use the RANS equations, which do not resolve the spatial and temporal characteristics of the boundary layer. In *Trolle et al.* [2008], for example, the SOD is fixed to 0.7 g m^{-2} day^{-1} as a calibration parameter for a one-dimensional water-quality model applied to Lake Ravn (Denmark). In the two-dimensional model applied by *Boegman et al.* [2008a] to Lake Erie, SOD = 0.55 g m^{-2} day^{-1} was used. When SOD is not directly assigned, a simple sediment oxygen flux model is employed that operates by assuming that the flux is only a function of the overlying water temperature and DO concentration (*static* model) [*Hipsey et al.*, 2006]. Using this model with a three-dimensional hydrodynamic driver, *Leon et al.* [2011] find good agreement with measured DO profiles in Lake Erie. Such models, however, do not capture any of the boundary layer physics and are still at an early stage of development.

[9] In spite of the availability of field measurements and experimental data, prediction of the various components of the oxygen budget throughout the water column still suffers from many deficiencies, including low-order turbulence modeling of transport dynamics and highly empirical definitions of biogeochemical parameters characterizing the organic sediment layer. Moreover, no successful attempt has been made to isolate the mechanisms governing DO transfer

from water to an organic sediment layer. There is also the need to assess physical assumptions and speculations underlying currently adopted solute-transport models in environmental flows. An investigation method that provides a more detailed description of the turbulent flow (both statistically and instantaneously) than what is available from experimental studies or field measurements, is needed for these purposes. Studies have shown that a full understanding of the biological responses to the varying thermo-fluid dynamic conditions requires physical and numerical models that couple hydro-dynamic transport and the dynamics of water quality and aquatic organisms at all the important scales [*Koseff et al.*, 1993; *Boegman et al.*, 2008b]. Being able to resolve the vertical distribution of DO with a fully coupled model would allow for the quantification of the SOD under various fluid flow conditions. The currently employed water-quality models, that tune the SOD such that modeled DO concentration match in-situ observations, would considerably benefit from a process-oriented parametrization of the SOD based on resolvable flow features in the near-wall region. There is no mechanistic model for SOD based on parameters resolved in currently adopted RANS models.

[10] Within such framework, the present work is aimed at developing a prediction and analysis tool to study oxygen-depletion dynamics with well established eddy-resolving numerical techniques that accurately reproduce the turbulent transport on the water side. Reliable turbulence modeling for the water side transport will help identify and quantify weaknesses in the components of the complete model where the characterization of the governing physical processes is still incomplete. We will focus our analysis on DO transport dynamics of the (non-stratified) near-bed region, and use a simple channel-flow model. Due to the wide range of scales exhibited by the velocity and scalar fields, resolving all the turbulent eddies is infeasible. Large-eddy simulations (LES) will be used to model the transport on the water side, while the diffusion and absorption model proposed by *Higashino et al.* [2008], together with Darcy's Law for pore water induced transport, will be used in the governing equations for the sediment side. In the following, we begin by describing the model, which includes the governing equations, the numerical method, and the coupling of the two layers. The comparison between the predictions of our model and the experimental results and a sensitivity test to some of the important model parameters will then be presented. Some remarks and suggestions for further work in this field conclude the article.

2. Problem Formulation

[11] In the present work we adopted the large-eddy simulation technique to model the momentum and scalar transport in the fluid, rather than the solution of the RANS equations, to avoid the errors associated with turbulence models and to capture local and instantaneous transport events not present in a RANS solution. Also, in LES only the smaller eddies are modeled, and the motions of the larger eddies (of size comparable to the integral scale) are directly computed extending the range of applicability of the model. In the following, first we discuss the governing equations

and the simulation parameters used for the solution of the governing equations in the fluid and in the sediment layer. We then present the computational setup, and the numerical method employed.

2.1. Momentum and Scalar Transport in the Fluid

[12] The filtered equations of conservation of mass and momentum can be obtained by applying a filtering operator $\overline{()}$ to the continuity and Navier-Stokes equations [*Leonard*, 1974]

$$\frac{\partial \overline{u}_i}{\partial x_i} = 0, \tag{1}$$

$$\frac{\partial \overline{u}_j}{\partial t} + \frac{\partial \overline{u}_i \overline{u}_j}{\partial x_i} = -\frac{\partial \overline{p}}{\partial x_j} - \frac{\partial \tau_{ij}}{\partial x_i} + \frac{1}{Re_b}\nabla^2 \overline{u}_j - f\delta_{1i}, \tag{2}$$

where x_1, x_2 and x_3 (or x, y and z) are, respectively, the streamwise, wall-normal and spanwise directions, δ_{ij} the Kronecker delta and $\overline{u}_i$ the filtered velocity components in those directions. The filter used is a top-hat filter composed of three one-dimensional 3-point discrete filters. These equations have been made dimensionless by using δ (the half-width of the channel) as a reference length scale, and U_b (the bulk velocity, i.e., the streamwise velocity averaged over the entire domain) as a velocity scale. The Reynolds number is, therefore,

$$Re_b = \frac{U_b \delta}{\nu}, \tag{3}$$

where ν is the kinematic viscosity of water. The forcing term f in the streamwise momentum equation represents the mean pressure gradient driving the flow. The sub-grid scale (SGS) stresses $\tau_{ij} = \overline{u_i u_j} - \overline{u}_i \overline{u}_j$ are parameterized by an eddy-viscosity model

$$\tau_{ij} - \delta_{ij}\tau_{kk}/3 = -2\nu_T \overline{S}_{ij}, \quad \nu_T = C\overline{\Delta}^2 |\overline{S}|, \tag{4}$$

where

$$\overline{S}_{ij} = \frac{1}{2}\left(\frac{\partial \overline{u}_i}{\partial x_j} + \frac{\partial \overline{u}_j}{\partial x_i}\right) \tag{5}$$

is the resolved strain rate tensor and $|\overline{S}| = (2\overline{S}_{ij}\overline{S}_{ij})^{1/2}$ is its magnitude; $\overline{\Delta} = (\Delta_x \Delta_y \Delta_z)^{1/3}$ is the filter width. The coefficient C is evaluated using the dynamic procedure [*Germano et al.*, 1991; *Lilly*, 1992], and averaged over planes parallel to the wall.

[13] Dissolved oxygen in water behaves like a passive scalar with very low diffusivity, compared with the kinematic viscosity. The filtered transport equation for DO is, therefore,

$$\frac{\partial \overline{c}}{\partial t} + \frac{\partial \overline{u}_i \overline{c}}{\partial x_i} = \frac{\partial}{\partial x_i}\left[\frac{1}{Sc\,Re_b}\frac{\partial \overline{c}}{\partial x_i} - J_i^{sgs}\right], \tag{6}$$

where $Sc = \nu/D$ is the Schmidt number and $\overline{c}$ is the instantaneous filtered scalar concentration field normalized with the bulk DO concentration C_b defined analogously to U_b.

The SGS scalar flux, J_i^{sgs}, is also parameterized by an eddy-diffusivity model

$$J_i^{sgs} = -\alpha_T \frac{\partial \overline{c}}{\partial x_i}; \qquad \alpha_T = C_D \overline{\Delta}^2 |\overline{S}|. \qquad (7)$$

The extension of the dynamic model [Germano et al., 1991; Lilly, 1992] to the scalar transport at high Schmidt numbers has been shown to be accurate by Zang et al. [1993], Calmet and Magnaudet [1997] and Na [2004]. For this reason we also used the dynamic procedure to determine the model coefficient C_D.

2.2. Momentum and Scalar Transport in the Sediment

[14] The normalized instantaneous DO concentration level in the sediment layer, c_s, is determined by more complex mechanisms. Dissolved oxygen is transported by diffusion, advection and dispersion, but also depleted by decomposing organic matter. The governing equation for c_s is

$$\frac{\partial c_s}{\partial t} + \frac{\partial}{\partial x_i}[u_{si} c_s] = \frac{\partial}{\partial x_i}\left[\left(\frac{1}{Sc_s Re_b} + D_e\right)\frac{\partial c_s}{\partial x_i}\right] - \dot{c}_s. \qquad (8)$$

A 'sediment Schmidt number' Sc_s can be defined as [Røy et al., 2004]

$$Sc_s = \nu/\varphi D_s, \qquad (9)$$

where φ is the sediment porosity, D_s is the effective molecular diffusivity for DO in the porous medium and u_{si} is the i-th component of the interstitial velocity field driven by the pressure gradients at the SWI generated by the overlying turbulent flow; the effective diffusivity D_e—representing dispersion effects—is commonly modeled as the product of a characteristic length scale, l_e, times a velocity scale, V_e [Freeze and Cherry, 1979]. In the present work we adopt the parametrization introduced by Higashino and Stefan [2011] for D_e by extending it to available local and instantaneous quantities obtaining

$$D_e = \varphi^2 d_s (u_{si} u_{si})^{1/2}, \qquad (10)$$

where d_s is the sediment grain size (proportional to the square root of permeability via the Kozeny-Carmen relationship [Bear, 1972]). The DO absorption by organic matter is represented by the sink term, $\dot{c}_s$, which must be parameterized.

[15] The formulation for the DO advective and diffusive fluxes used here was proposed by Boudreau and Jørgensen [2001]. The effective diffusion coefficient inside the sediment, D_s, is lower than in water because molecules must follow a tortuous path around sediment grains. Also, the resulting flux must be reduced by a factor φ to account for the pore-space fraction available to transport in pore water. Several empirical correlations exist between D_s, D and φ [Boudreau, 1996; Iversen and Jørgensen, 1993]. By using such relationships and the mass conservation constraint at the sediment-water interface (SWI),

$$\frac{1}{Sc_s Re_b}\left(\frac{\partial c_s}{\partial y}\right)_{SWI} = \frac{1}{Sc Re_b}\left(\frac{\partial c}{\partial y}\right)_{SWI}, \qquad (11)$$

it is possible to retrieve the value of the sediment porosity in (9) from the measurable slope discontinuity in the mean

oxygen profiles at the SWI. The values of porosity used in this paper are calculated based on the correlation between D_s, D and φ adopted in Higashino et al. [2009] and Higashino and Stefan [2011].

[16] The magnitude of the interstitial flow in the porous medium depends on the permeability. When inertial effects for the fluid occupying the sediment pore-spaces are negligible (for effective grain size, for example, smaller than 1 mm) the flow inside the sediments can be described by Darcy's Law

$$u_{si} = -K Re_b\left(\frac{\partial p_s}{\partial x_i} + f \delta_{i1}\right), \qquad (12)$$

where

$$K = K^*/\delta^2; \quad p_s = P_s^*/(\rho U_b^2). \qquad (13)$$

[17] Here P_s^* is the total pressure, including the gravitational potential, ρ is the density of the water, K^* is the intrinsic permeability of the sediment, and p_s is the normalized pore pressure. The latter can be obtained by combining Darcy's Law (12) with the incompressibility constraint for pore water flow

$$\frac{\partial u_{si}}{\partial x_i} = 0, \qquad (14)$$

yielding

$$\nabla^2 p_s = 0. \qquad (15)$$

[18] Following Higashino et al. [2008], the non-linear sink term $\dot{c}_s$ is parameterized as

$$\dot{c}_s = Re_b \mu_\chi \frac{c_s}{K_{O_2} + c_s}\chi, \qquad (16)$$

where

$$\mu_\chi = \frac{\mu_\chi^* \nu}{U_b^2}; \quad K_{O_2} = \frac{K_{O_2}^*}{C_b}; \quad \chi = \frac{\chi^*}{Y_c C_b}. \qquad (17)$$

The parameters used in (17) are μ_χ^*, maximum specific DO utilization rate (in day^{-1}), $K_{O_2}^*$, half-saturation coefficient for DO utilization (in mg l^{-1}), Y_c effective yield for the microbial utilization of DO and χ^*, the value of biomass concentration of aerobic heterotrophs (oxygen absorbing organisms). The values of these constants have been taken from Higashino et al. [2008], and are summarized in Table 1. The corresponding dimensionless quantities are reported in Table 2.

[19] The oxygen absorption rate is taken to be proportional to the level of biomass concentration of oxygen-consuming bacteria, χ, a time dependent quantity whose evolution an be described by a simple logistic model for population growth, giving

$$\frac{d\chi}{dt} = \left(Re_b \mu_\chi \frac{c_s}{K_{O_2} + c_s} - k_d\right)\left(1 - \frac{\chi}{\chi_{max}}\right)\chi, \qquad (18)$$

Table 1. Dimensional Fluid Flow and Biogeochemical Parameters for Oxygen Uptake Model

Parameter	Description	Typical Range	Value Adopted
μ_χ^* (day^{-1})	DO utilization rate	0.72–13.2	2.4
$K_{O_2}^*$ (mg l^{-1})	half-saturation coefficient for DO utilization	0.2	0.2
χ^* (mg l^{-1})	concentration of aerobic heterotrophs	100–300	700
k_d^* (day^{-1})	first order decay coefficient of χ^*	0.1	0.1
D (10^{-9} m^2 s^{-1})	molecular diffusivity of DO	1.2–1.7	2.0–3.0
ν (10^{-6} m^2 s^{-1})	kinematic viscosity	1.1–1.5	0.7–0.9
δ (cm)	half-channel height	–	7.6
δ_s (cm)	sediment-layer thickness	–	2.5
U_b, U_∞ (cm s^{-1})	bulk and maximum velocity	1–20	5–10
C_b, C_∞ (mg l^{-1})	bulk and maximum DO concentration	6–13	2–8.2
K^* (cm^2)	intrinsic permeability	10^{-8}–10^{-6}	10^{-6}–10^{-5}

where k_d is the normalized first-order decay coefficient

$$k_d = k_d^* \delta/U_b. \tag{19}$$

For the commonly adopted values of the parameters on the right-hand side of (18), it can be shown that the timescale over which variations of χ become significant is of the order of days. Since our simulations span much shorter times, we will assume a constant value of χ and ignore (18), an approach also followed by *Higashino et al.* [2008].

2.3. Computational Setup

2.3.1. Numerical Model

[20] The computational setup used is shown in Figure 1. The flow is driven by a pressure gradient $f\, \delta_{1i}$, which is constant in space and adjusted in time to maintain a constant mass flux. The governing equations (1), (2) and (6) are solved on a Cartesian domain. In the streamwise and spanwise directions, x and z, periodic boundary conditions are used for all quantities. At the upper and lower walls, the velocity obeys no-slip conditions; for the scalar we use Neumann conditions, with assigned flux. The oxygen dynamically absorbed by the sediment layer across the SWI is reinserted in the flow, at the same rate, from the top boundary by means of an imposed instantaneous flux. Thus, the value of the volume averaged DO concentration is maintained constant and equal to the reference value C_b. The oxygen flux assigned at the SWI is calculated based on the coupling between the water and sediment layers, and will be discussed later.

[21] Two differences exist between the present computational setup and the experimental one used by *O'Connor and Hondzo* [2008]. First, they used a square duct, while we have a plane channel, with no sidewalls. Second, in the experiment, re-aeration is prevented; thus, the oxygen content slowly decreases when the flume is running; when the flow is quiescent, the DO flux to the sediment layer is negligible. In our calculations, the oxygen content is steady in time, so that a statistical steady state can be achieved. This allows to obtain converged statistical samples more rapidly than if an unsteady calculation were carried out, and ensemble averages were taken.

[22] The numerical model used to compute the flow on the water side is a well-validated finite difference code [*Keating et al.*, 2004], based on a staggered grid. Second-order central differences are used for both convective and diffusive terms. The time advancement scheme is a Crank-Nicolson scheme for the wall-normal diffusive term, and a low-storage 3rd-order Runge–Kutta method for the other terms. The solution of the Poisson equation is obtained by Fourier transform of the equation in the spanwise and streamwise direction, followed by a direct solution of the resulting tridiagonal matrix, at each wave number. The code is parallelized using the Message Passing Interface (MPI) protocol.

[23] The equations in the sediment layer are solved with the same numerical approach. The scalar and pressure field are located at the cell center and the velocity components at the staggered positions, on the faces of the DO control volumes. The scheme has the same numerical accuracy and stability as the one used on the water side.

[24] An important aspect of the present work is the coupling between the water and sediment layers. We developed a coupling procedure that can enforce the continuity of both the mass flux and the value of oxygen concentration at the

Table 2. Dimensionless Fluid Flow and Biogeochemical Parameters for Oxygen Uptake Model

Parameter	Description	Typical Range	Value Adopted
Re_b, Re_{max}	$Re_b = U_b\delta/\nu$, $Re_{max} = U_\infty\delta/\nu$	10^3–10^6	10^3–10^4
Re_τ	$Re_\tau = u_\tau\delta/\nu$	180–1000	241–630
Sc	$Sc = \nu/D$	650–1000	188–360
φ	sediment layer porosity	0.3–0.7	0.55
ν_T, α_T	eddy viscosity and diffusivity	–	–
μ_χ	$\mu_\chi = \mu_\chi^*\nu/U_b^2$	–	0.467–2.4 ($\times 10^{-7}$)
K_{O_2}	$K_{O_2} = K_{O_2}^*/C_b$	–	0.024–0.1
Y_c	effective yield for DO utilization	0.83–1.17	1.0
χ	$\chi = \chi^*/Y_c C_b$	–	85.4–350
k_d	$k_d = k_d^*\delta/U_b$	–	0.076–0.152
K	$K = K^*/\delta^2$	–	1.7×10^{-8}–1.7×10^{-7}
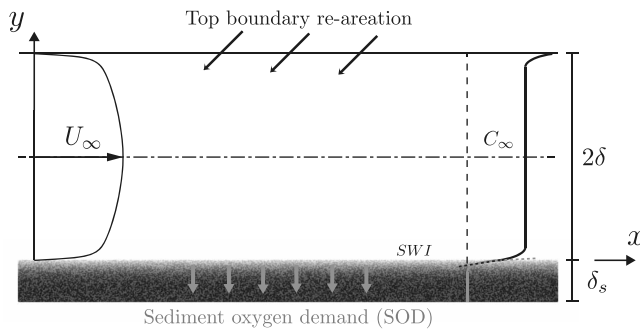
Figure 1. Computational setup. The diffusive sublayer thickness is exaggerated for visualization purposes. The value of oxygen concentration outside the diffusive sublayer coincides with the bulk concentration $C_\infty = C_b$.

SWI. This allows the implicit time-advancement of the solution in both layers (which is required to avoid the viscous time step limitation caused by the highly stretched meshes near the SWI) while algebraically independent calculations are performed in the two separate computational domains (water and sediment); thus guaranteeing modularity and simplicity in the implementation of the numerical scheme. The details of the implementation are described in Appendix A; here, we only summarize the procedure. The oxygen concentration is updated only at the SWI with an explicit scheme taking into account contributions to the flux from both the water side and the sediment side. The resulting predicted value is used to impose an implicit, Dirichlet boundary condition to update the DO distribution in the sediment layer. Then, a Neumann boundary condition to satisfy the mass conservation constraint (11) can be imposed on the scalar field on the water side. The next step is to update the velocity field on the water side and use the updated pressure field to drive the interstitial flow in the sediment layer (12).

[25] Note that the above procedure results in a time lag (by a fraction of the time step Δt) between the solution in the water and sediment layer. Since transport dynamics at the SWI exhibit much longer timescales than those in the fluid, the decoupling does not affect the time accuracy of the numerical model: typical values of Δt, in our simulations, correspond to 1–10 ms of real time.

2.3.2. Experimental and Field-Scale Parameters

[26] The numerical study (and, in particular, the range of parameters used) was designed to allow direct comparison to the laboratory data from *O'Connor and Hondzo* [2008]. The flow parameters adopted in these experiments are summarized in Table 3. We performed numerical simulations matching the fluid dynamic conditions of the experiments indicated as LES-2, LES-3, LES-4 and LES-5 and the respective parameters are summarized in Table 4. Then, only

for case LES-3, runs have been repeated at $\chi^* = 500$ mg/1 and $\chi^* = 1000$ mg/1, keeping $\varphi = 0.55$ and $K^* = 0$. Also, for the same case, the sediment properties have been kept constant at $\chi^* = 700$ mg/1, $\varphi = 0.55$ and $K^* = 0$ and Re_b has been changed to $Re_b = 3000$ and then to $Re_b = 9000$, by only changing U_b. Finally, for the LES-4 case the effects of permeability have been investigated for $K^* = 10^{-6}$ cm^2 and $K^* = 10^{-5}$ cm^2.

[27] The actual fluid flow characteristics in oceanic environments may differ from the experimental and numerical simulations. Bottom waters can be significantly colder, resulting in a much higher Schmidt number (typically of the order of 1000 for $T = 8°C$ [*Bryant et al.*, 2010]). The sediment layer surface may not be flat and large scale roughnesses may be present such as mounds, sand ripples and dunes which play an important role in determining advective solute exchange across the SWI [*Boudreau and Jørgensen*, 2001]. In small alpine lakes, typically measured free stream and bed shear velocities may be of the order of 0.05 m s^{-1} and 0.001 m s^{-1}, respectively [*Bryant et al.*, 2010; *Lorke et al.*, 2003], which are actually lower than what realized experimentally (0.1 m s^{-1} and 0.005 m s^{-1}, respectively). For lakes such as Lake Erie, free-stream velocities in the range of 0.01 m s^{-1} to 10 m s^{-1} can be observed [*Bedford and Abdelrhman*, 1987]. In costal environments current velocities up to 0.12 m s^{-1} have been observed by *Chriss and Caldwell* [1982] and up to 0.8 m s^{-1} at the edge of tidal bottom boundary layers [*Sanford and Lien*, 1999]. Moreover, even if in experimental and numerical studies the velocity scales were to be matched, the length scales of the large eddies governing the transport in the outer region can be of the order of meters in lakes and kilometers in oceans which lead to much higher Reynolds numbers (up to 10^9 [*Hendry and Wunsch*, 1973]) than what are reproducible in laboratory or numerical experiments. The thickness of the diffusive sublayer for DO is of the order of millimeters in both field scale and experiments. *Bryant et al.* [2010] measured thicknesses up to 1 cm due to an abrupt decrease of the turbulent mixing intensity. In spite of these differences, the purpose of this work is to validate the complete model by comparing it to lab experiments, which were performed in freshwater and at higher temperatures, resulting in lower Schmidt numbers with smooth cohesive sediments and Reynolds numbers in the range $3 - 10 \times 10^3$.

2.3.3. Simulation Parameters

[28] The computations were carried out using domain sizes, on the water side, of dimensions ranging between $16 \times 2 \times 8$ (for the low-Re_b cases) and $6 \times 2 \times 3$ (for the high-Re_b ones); recall that all quantities are normalized by δ, the channel half-width, which in this case is 7.6 cm. The number of grid points used varied between cases, resulting in a streamwise grid spacing, in wall units (indicated by a plus), of $\Delta x^+ \simeq 26$ for all cases and in a variable spanwise

Table 3. Flow Characteristics of Recirculating Flume Experiments EXP-2 to EXP-5 in *O'Connor and Hondzo* [2008][a]

Experiment	T (°C)	ν(cm^2 s^{-1})	D(cm^2 s^{-1})	U_{max} (cm s^{-1})	u_τ (cm s^{-1})	C_b(mg l^{-1})	Re_{max}	Sc
EXP-2	26	0.88×10^{-2}	2.46×10^{-5}	5.25	0.25	8.2	4534	358
EXP-3	30	0.80×10^{-2}	2.75×10^{-5}	7.50	0.34	5.8	7124	291
EXP-4	35	0.70×10^{-2}	3.21×10^{-5}	9.50	0.43	4.5	10,314	218
EXP-5	37	0.65×10^{-2}	3.45×10^{-5}	11.00	0.50	2.0	12,861	188

[a]Estimates of C_b have been extracted from *Higashino et al.* [2008] by matching the steady solution of (8) in the sediment layer.

Table 4. Summary of LES Parameters Matching Experimental Flow Conditions (Table 3)[a]

LES Run	Re_b	Re_τ	Re_{max}	Sc	χ^* (mg l^{-1})	K^* (cm^2)	Domain Size	Grid
LES-2	3900	241	4534	358	700	0	$12 \times 2 \times 6$	$128 \times 128 \times 128$
LES-3	6137	360	7124	291	700	0	$8 \times 2 \times 4$	$128 \times 128 \times 128$
LES-3 (low-Re)	3000	188	3500	291	700	0	$16 \times 2 \times 8$	$128 \times 128 \times 128$
LES-3 (high-Re)	9000	510	10,500	291	700	0	$6 \times 2 \times 3$	$128 \times 128 \times 128$
LES-3 (low-χ)	6137	360	7124	291	500	0	$8 \times 2 \times 4$	$128 \times 128 \times 128$
LES-3 (high-χ)	6137	360	7124	291	1000	0	$8 \times 2 \times 4$	$128 \times 128 \times 128$
LES-4	9019	515	10,314	218	700	0	$6 \times 2 \times 3$	$128 \times 192 \times 256$
LES-4 (K-6)	9019	515	10,314	218	700	10^{-6}	$6 \times 2 \times 3$	$128 \times 192 \times 256$
LES-4 (K-5)	9019	515	10,314	218	700	10^{-5}	$6 \times 2 \times 3$	$128 \times 192 \times 256$
LES-5	11,285	630	12,861	188	700	0	$6 \times 2 \times 3$	$128 \times 192 \times 256$

[a]See Tables 1 and 2 for parameter definitions.

resolution ranging from $\Delta z^+ \simeq 12$ to $\Delta z^+ \simeq 6$ where $\Delta x^+ = u_\tau \Delta x / \nu$ and $\Delta z^+ = u_\tau \Delta z / \nu$. This resolution is nearly fine enough to resolve the scales responsible for the dissipation of turbulent kinetic energy; because of the high Sc, however, a range of sub-Kolmogorov scales exists in the DO field that require finer resolution. Previous studies of high-Sc scalar transport in a turbulent channel flow (*Calmet and Magnaudet* [1997] and *Bergant and Tiselj* [2007] both modeled the smallest scalar scales with a sub-grid scale model) show that low-order statistics can be captured very accurately even on coarse grids, and that spectra and scalar variance profiles in the diffusive sublayer and the scalar buffer layer ($y^+ < 5$) are unaffected by the cutoff of sub-Kolmogorov scales. Another issue brought about by the low scalar diffusivity of oxygen is the thinning of the diffusive sublayer; the ratio of diffusive-sublayer thickness to viscous-sublayer thickness scales like Sc^{-n}, with $0.5 > n > 0.3$ [*Dong et al.*, 2003; *Schwertfirm and Manhart*, 2007; *Lorke et al.*, 2003]. This results in the need of finer wall-normal resolution near the solid boundaries.

[29] On the sediment side, in all cases, 65 points have been used in the vertical direction, for a sediment layer depth of $\delta_s = 0.33\delta$ and the porosity has been set to $\varphi = 0.55$. Spanwise and streamwise resolution and box size are the same as the water side.

3. Results and Discussion

### 3.1. Validation and Grid Convergence Test

[30] To validate the velocity statistics we compare in Figure 2 the mean velocity and trace of the Reynolds-stress tensor $q^2 = \langle u'_i u'_i \rangle$ with direct simulation data at comparable Reynolds numbers [*Moser et al.*, 1999]. All quantities are normalized by u_τ and ν, and are averaged spatially over planes parallel to the wall and in time over 240 samples for a total averaging of 1200 δ/U_b time units for the low Re_b case, and 400 time units for the high Re_b. To test for grid convergence of the scalar statistics we compare in Figure 3 LES of passive-scalar transport at $Re_\tau = 400$ with progressively refined grids to asses the effects of the unresolved scales on the resolved quantities for the scalar. Neumann boundary conditions were applied at the solid wall for this test. The results confirm that first-order moments are insensitive to the grid resolution, provided that the diffusive sublayer, whose thickness is known *a priori* in channel flow, is resolved. A slight grid dependency can still be observed in the scalar variance profiles which collapse, for every grid, over more than 99% of the channel height, varying only in part of the

diffusive sublayer (by 5% in the last refinement step) where scalar fluctuations are inactive and not statistically relevant for transport dynamics. The presence of the sediment layer, which damps oscillations via the sink term (16), is expected to improve the near-wall convergence.

3.2. Instantaneous Flow Characteristics

[31] We want to highlight the three-dimensional and instantaneous nature of the data generated by the LES by looking at visualizations extracted from case LES-4 (K-6), which includes all the transport processes that have been implemented in our model. Data from a RANS simulation of the same problem would be steady and one-dimensional (all quantities vary only along y) and would not allow for the analysis of the flow features, which exhibits a multiplicity of scales both in space and time.

[32] The spatial distribution of the diffusive flux at the SWI (Figure 4a) reveals very fine organized structures,
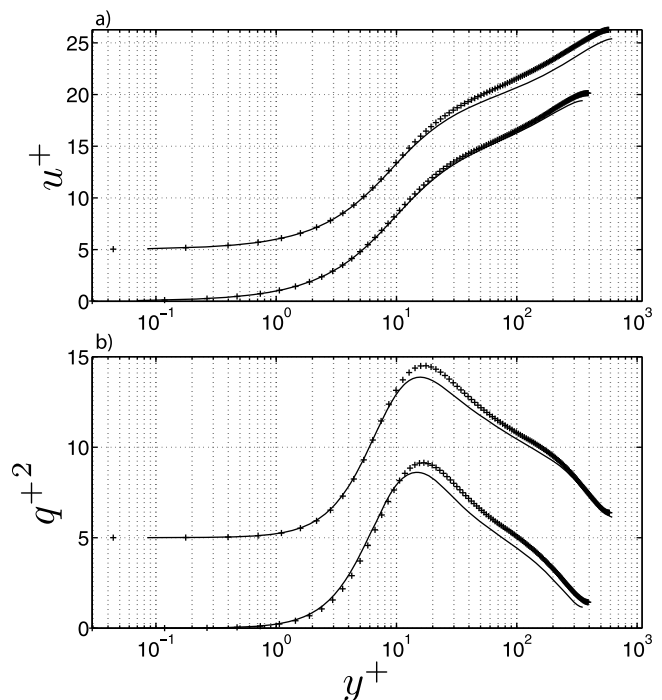
Figure 2. Profiles of (a) mean velocity and (b) q^2. LES (solid line) at $Re_\tau = 360$ and $Re_\tau = 630$; direct simulation (pluses) at $Re_\tau = 395$ and $Re_\tau = 600$ [*Moser et al.*, 1999]. Each profile is shifted vertically by 5 units for clarity.
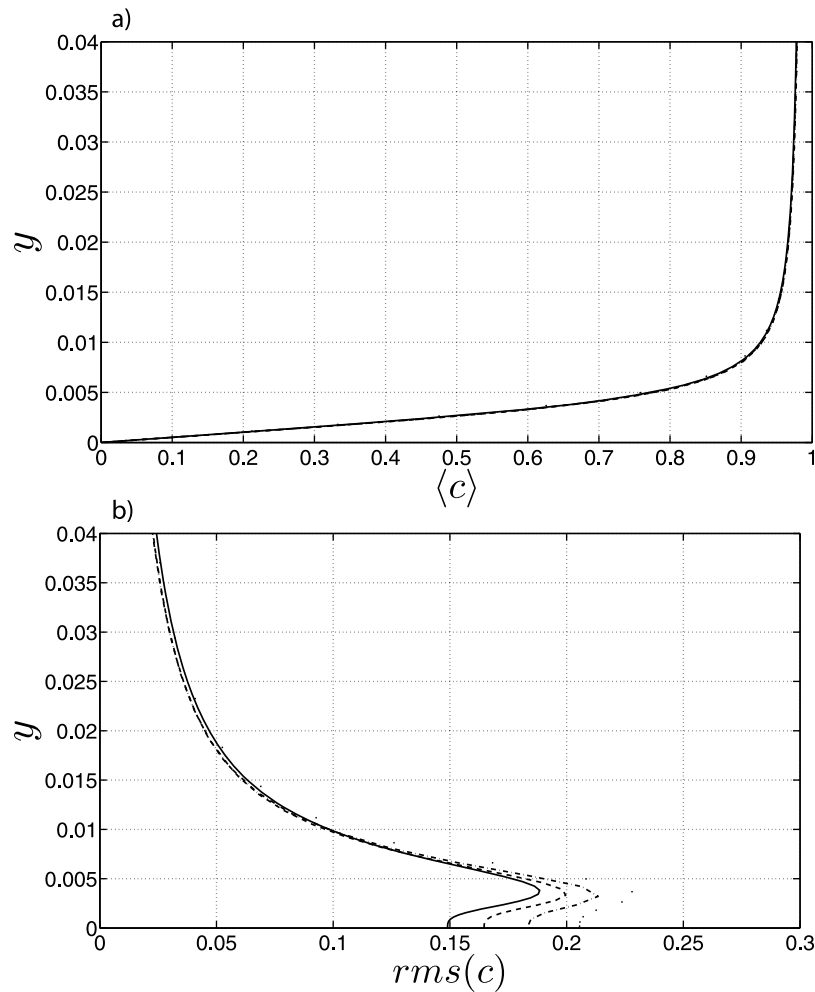
Figure 3. Grid convergence test for scalar transport at $Sc = 300$ and $Re_\tau = 400$. (a) Mean profiles and (b) (resolved) scalar fluctuation intensity profiles for grid size 64^3 (dotted line), 96^3 (dash-dotted line), 128^3 (dashed line), 192^3 (solid line).

similar to the ones observable in the DO concentration contours (Figure 4b) and in the vertical velocity fluctuations (Figure 4c) at $y = 0.01$; this is the edge of the diffusive sublayer, which can be identified as the location where the turbulent flux reaches its freestream value (shown later). Vertical velocity fluctuations here play an important role in the transport governed by turbulent motions convecting, on average, patches of high DO concentration toward the SWI and low DO concentration toward the bulk flow.

[33] Contours of instantaneous velocity and scalar fluctuations have also been extracted in the plane $y = -0.0025$ in the sediment layer (Figure 5). The scalar field exhibits the same elongated structure in the streamwise direction both above (Figure 4b) and below (Figure 5b) the SWI. The pore water-flow-enhanced effective diffusion in the porous medium (relative here to a permeability of $K^* = 10^{-6}\,\mathrm{cm}^2$ or $K = 1.7 \times 10^{-8}$) smooths out spatial gradients in the scalar field whereas higher levels of fluctuation intensity on the water side, especially due to spanwise variations in DO concentration, are evident from the visualizations; in spite of the overall higher variance, relatively extended regions of (approximately) constant DO concentration are visible on the water side. This is the signature of internal intermittency

effects, which are emphasized in the high-Sc limit [*Antonia and Orlandi*, 2003]; intermittency cannot occur in the sediment layer, where no scalar-variance-production mechanisms are present. The velocity fluctuation field does not preserve its structure in the sediment layer, where it becomes more disorganized. This is due to the elliptic nature of the equations governing the advective transport here (15): the higher wave numbers are damped faster with depth, and, in this case, the signature of the pressure gradients, driving the flow at the SWI, disappears rapidly as the fluid penetrates into the permeable layer. The velocity and scalar field in the sediment appear rather uncorrelated as confirmed later.

3.3. Comparison With Experimental Data

[34] We now compare predictions of the present model with the experimental results reported by *O'Connor and Hondzo* [2008]. We attempt to reproduce the flow characteristics of experiments EXP-2, EXP-3, EXP-4 and EXP-5 (Table 3), which were carried out over several months and the water temperature varied from $T = 25°C$ to $T = 37°C$, with our model runs LES-2, LES-3, LES-4 and LES-5, respectively (Table 4). Kinematic viscosity and oxygen molecular diffusivity were both affected by the changes in
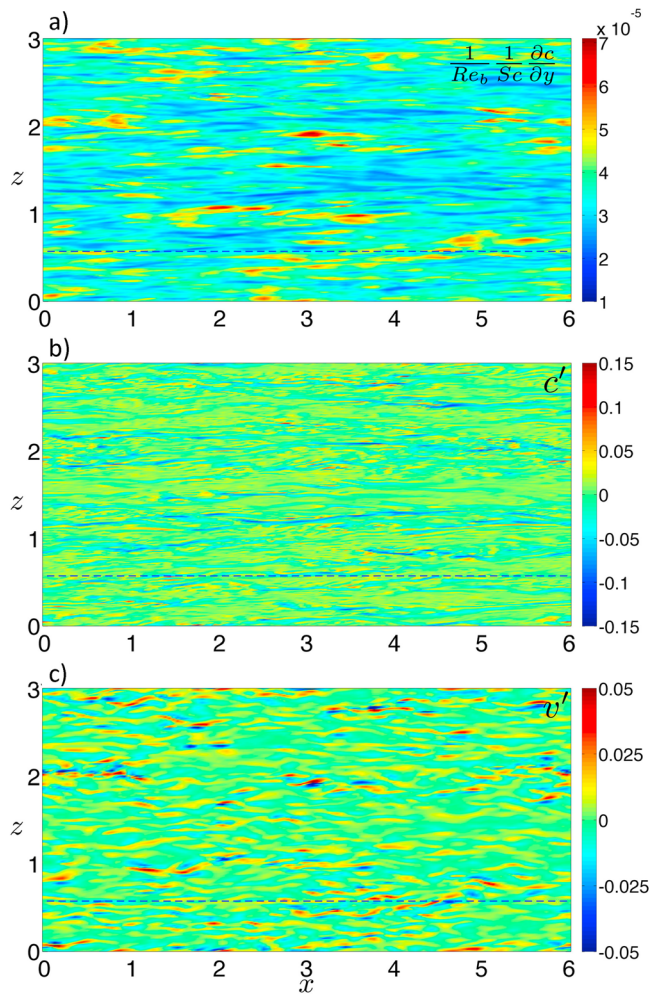
Figure 4. Contour plots of (a) diffusive flux at SWI, (b) scalar concentration fluctuations and (c) vertical velocity fluctuations at edge of the diffusive sublayer ($y = 0.01$ plane), for case LES-4 (K-6). The location of the $z = 0.57$ plane is indicated with a dashed black line. Note that the DO flux is scaled with $C_b U_b = 0.37$ mg l^{-1} m s^{-1}, the oxygen concentration field with $C_b = 4.5$ mg l^{-1}, the velocity fluctuating field with $U_b = 8.3$ cm s^{-1} and the coordinates x, z with $\delta = 7.6$ cm.

temperature, resulting in Schmidt numbers decreasing, in time, from 358 to 188. The water, with an initial homogeneous oxygen concentration, was forced to recirculate in a square duct over an artificially created organic sediment layer. The bulk decay of oxygen in the recirculating water during each experiment is ignored as it occurs over timescales much longer than the measurements and our numerical simulations; therefore, we maintain C_b constant for each experiment. DO-concentration profiles were experimentally measured in both water and sediment. The position of the sediment-water interface was determined from the gradient discontinuity in the mean oxygen profile, after an initial optical inspection. Experiment EXP-1 was not considered in our study, since (due to the low Reynolds number) the flow was probably transitional in the experiment (see the discussion in *Higashino et al.* [2008]). The fluid dynamic conditions in our model were set to match the centreline velocity,

the viscosity and oxygen diffusivity, the duct height and the sediment depth of the reference experiments (a discussion on the effects of the duct geometry is included below). Values of intrinsic permeability in the experiment are not given and are difficult to estimate, even when the sediment composition is given. Therefore, in our model, we first neglected the effects of pore water flow (12) or, equivalently, we set $K^* = 0$. Values of porosity and bacterial population were calibrated by matching the numerical results against data for EXP-2; the resulting values ($\chi^* = 700$ mg/l and $\varphi = 0.55$) were used for all the calculations. Note that the value of χ^* is somewhat larger than those typically found in the literature (Table 1) but smaller than the value $\chi^* = 1000$ mg/l used in the RANS calculations of *Higashino et al.* [2008]. Also, the uncertainty on the value of μ_χ^* (see Table 1) is rather high and affects the product $\chi \mu_\chi$ (or $\chi^* \mu_\chi^*$) in (16), which is the only parameter that ultimately matters for the sediment oxygen uptake.

[35] In Figure 6a we compare the mean concentration profile computed from the LES-2 run with the experimental data for case EXP-2 ($Re_{max} = 4500$ and $Sc = 360$). Since this case is used to determine the values of χ^* and φ, the calculations give good agreement (by design) with the experiments. In Figure 6b we present the same comparison between simulations and experiments for EXP-3 ($Re_{max} = 7100$ and $Sc = 290$). The agreement is still very good; in particular, the model predicts the correct DO penetration depth into the sediments and thickness of the oxygen diffusive sublayer. The value of the error bar at the SWI was
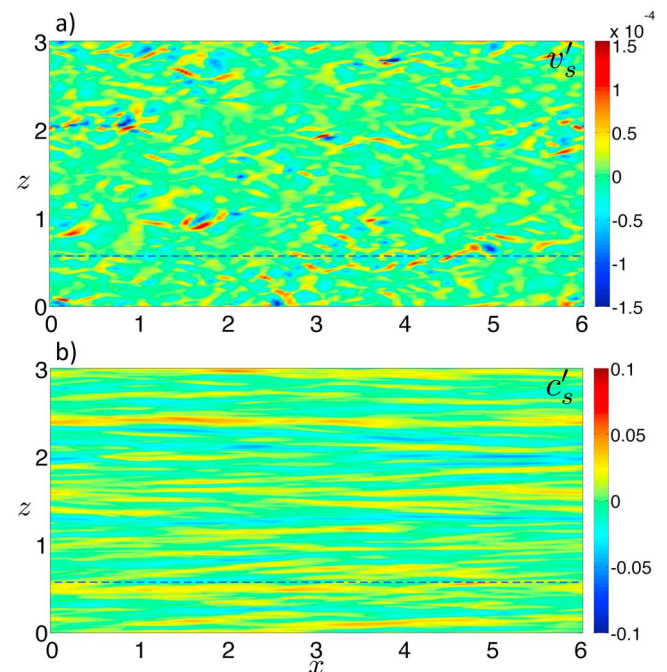
Figure 5. Contours of (a) vertical interstitial velocity and (b) scalar concentration at $y = -0.0025$ for case LES-4 (K-6). The location of the $z = 0.57$ plane is indicated with a dashed black line. Note that the velocity fluctuating field is scaled with $U_b = 8.3$ cm s^{-1}, the oxygen concentration field with $C_b = 4.5$ mg l^{-1} and the coordinates x, z with $\delta = 7.6$ cm.
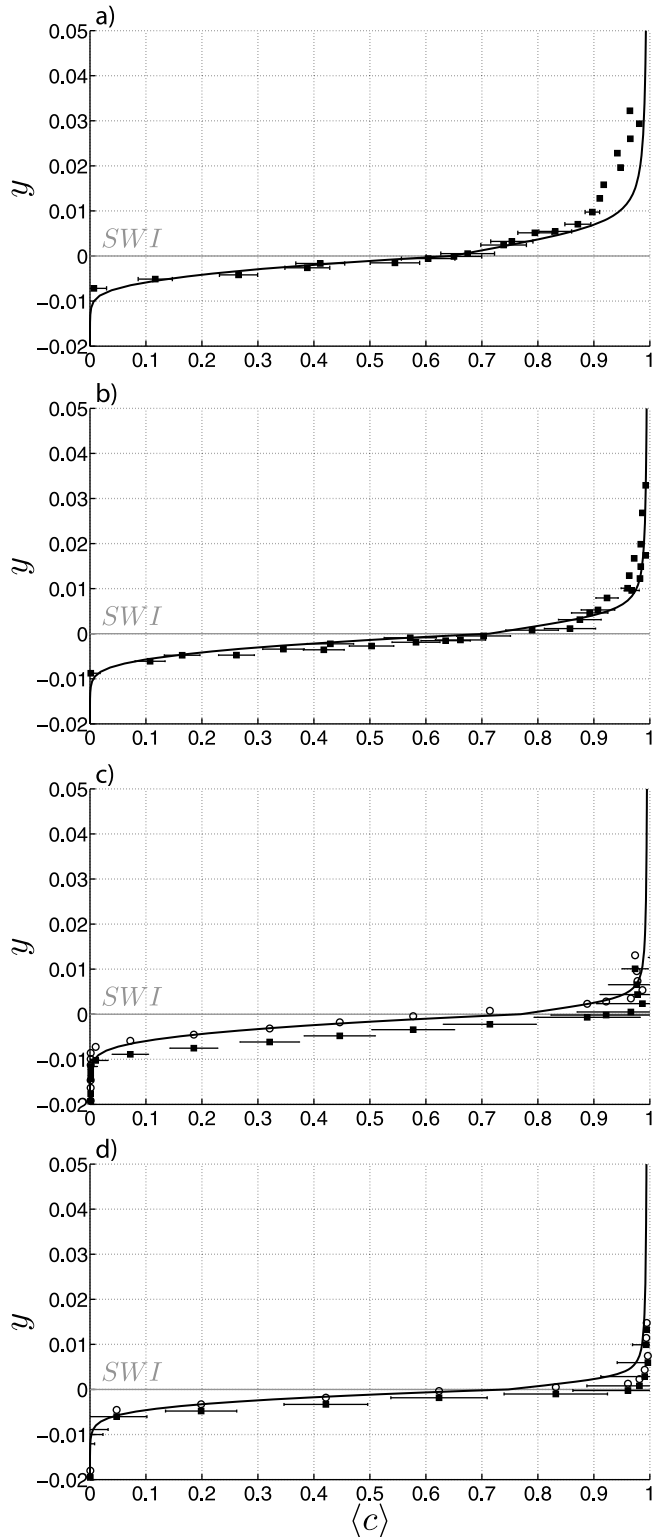
Figure 6. Comparison between the channel flow model (solid line) and experiments (squares) for cases (a) LES-2 and EXP-2, (b) LES-3 and EXP-3, (c) LES-4 and EXP-4 and (d) LES-5 and EXP-5. Circles are experimental results shifted upwards by 0.003δ (0.23 mm) in Figure 6c and 0.0015δ (0.11 mm) in Figure 6d.

taken from Figure 9 of *Higashino et al.* [2008], and reduced with the distance from the SWI, consistent with Figure 1 in *Røy et al.* [2004].

[36] When the Reynolds number is further increased, however, the quality of the agreement begins to deteriorate (see the comparison between LES-4 and LES-5 with EXP-4 and EXP-5 in Figures 6c and 6d). In the experimental results, as the Reynolds number increases, the position of the SWI becomes less defined and the increasing experimental uncertainty does not allow an accurate estimate of the material properties needed to run the numerical model, specifically the porosity, calculated from the experimental mean gradient discontinuity at the SWI. To establish if experimental uncertainty in the determination of the position of the SWI could have contributed to the observed disagreement, the experimental profiles from EXP-4 and EXP-5 were shifted vertically until the best match was found with the model predictions LES-4 and LES-5. This is obtained with a vertical shift of $+0.003$ δ (0.23 mm) and $+0.0015$ δ (0.11 mm), respectively, for EXP-4 and EXP-5 (shifted data are shown with open circles and no error-bars). These values are well within measurement error. Acceptable agreement is recovered between LES-4 and EXP-4 after the shifting, but the gradient discontinuity at the SWI (which is always present in our model and is governed by the porosity) is barely distinguishable, especially for EXP-5, in the experimental data. The fact that the discontinuity becomes gradually less defined in the measured data as Re is increased cannot be attributed to pre-resuspension phenomena such as bed-load transport, since estimates for the values of the mobility Shields parameter for the EXP-4 and EXP-5 experiments are below the critical level (see *Quaresma et al.* [2007] and *Boegman and Ivey* [2009]).

[37] While we believe the present model for the transport on the fluid side to be accurate, an improved biogeochemical model for the DO transport and absorption may be required. The sediment layer may have porosity, permeability and bacterial population variable, for example, with depth which can affect the predicted oxygen profile dramatically. These variations could be easily implemented in the model but, at this stage, any functional form adopted for these material properties would be completely arbitrary and specific measurements are required. The disagreement between numerical and laboratory data can, therefore, be solved in the framework of a collaborative approach between numerical modelers and experimentalist. The following sections explore the model's sensitivity to the governing fluid dynamic and geochemical parameters in an attempt to explain the observed discrepancies and investigate the simulated physics of transport.

3.4. Effects of Microbial Biomass Concentration

[38] The effect of the bacterial population χ^* on the oxygen concentration is examined in Figure 7. Variations up to 100 % of the bacterial population (from case LES-3 (low-χ) to case LES-3 (high-χ)) only result in a limited variation of the value of dissolved oxygen at the sediment-water interface (less than 10 %). On the other hand, the SOD, coinciding with the freestream value of the turbulent flux in Figure 7c, exhibits an almost linear dependency from χ^*. Increasing the value of the bacterial population by 40%, from case LES-3 (low-χ) to case LES-3, and by 43%, from
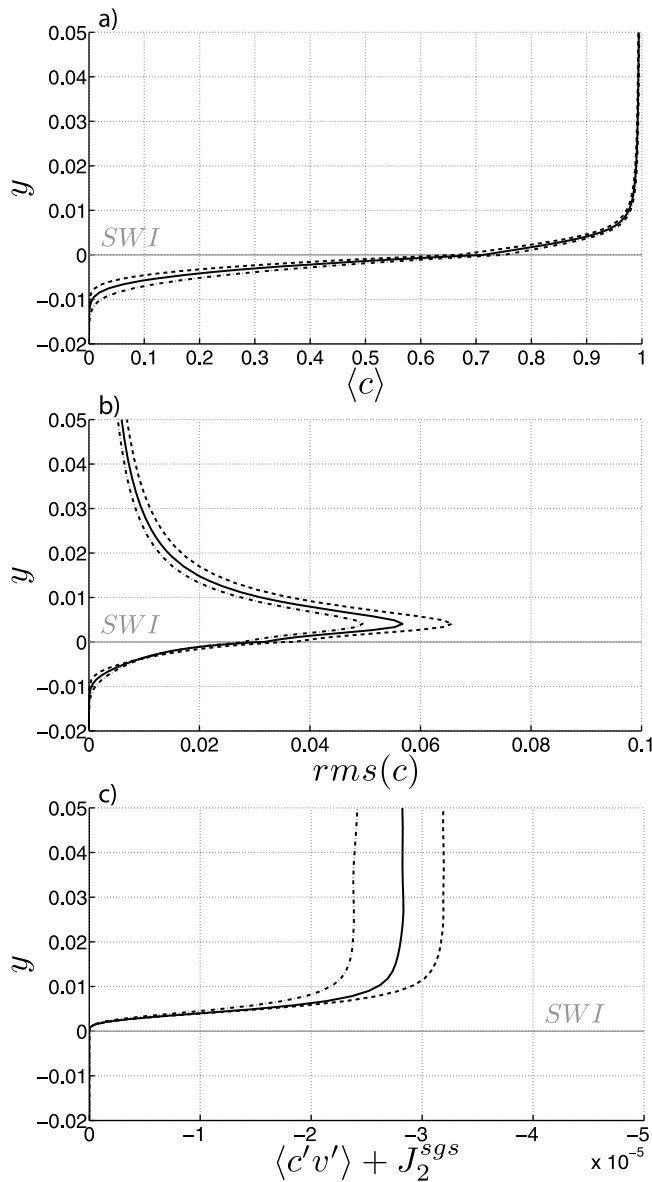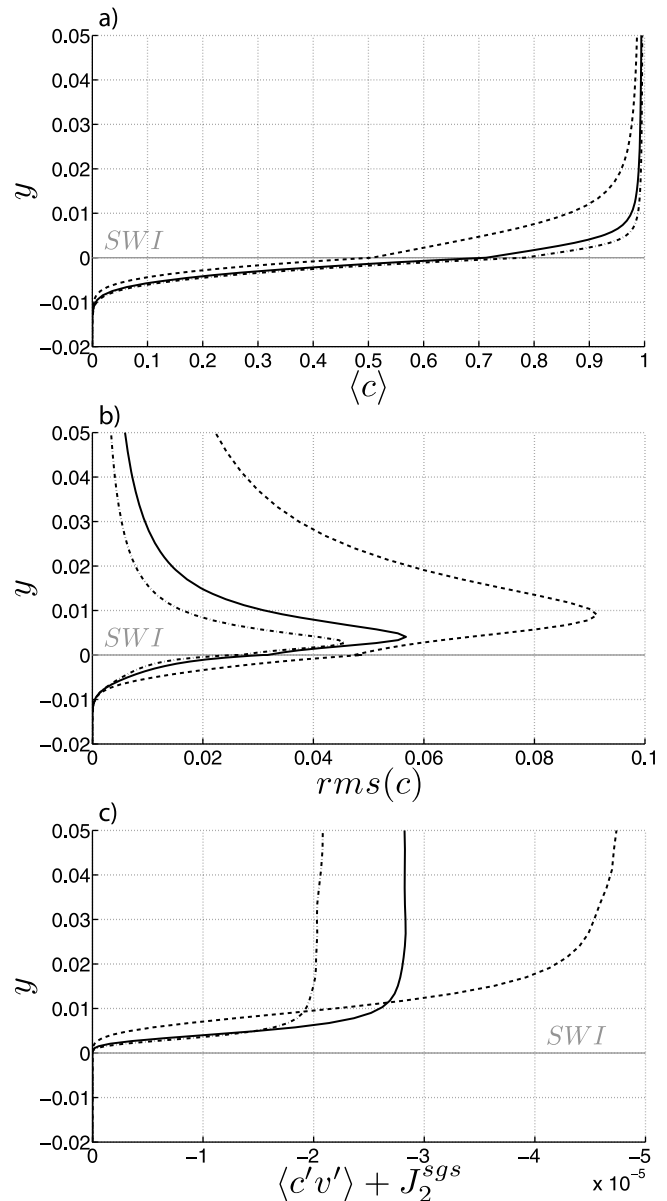
Figure 7. Effect of χ: (a) Mean scalar profile, (b) RMS intensity and (c) total turbulent flux. LES-3 (low-χ) is the dash-dotted line, LES-3 is the solid line and LES-3 (high-χ) is the dashed line.

LES-3 to LES-3 (high-χ), determines an enhancement of the SOD by approximately 17% and 14%, respectively. Sources of non-linearity are, however, present in the functional form used for the absorption term (16), often simplified to a constant term in field-scale applications [*Lorke et al.*, 2003; *Bryant et al.*, 2010], and intrinsically present in the turbulent transport dynamics on the water side. Values of resolved scalar RMS increase with χ^*, consistent with what is observed in field data [*Lorrai et al.*, 2010].

3.5. Effects of Reynolds Number

[39] In Figure 8 we show the effects of increasing flow velocity (and Reynolds number) on DO concentration for bulk Reynolds numbers of 3000, 6100 and 9000. This corresponds to an overall increase in the friction velocity (or Re_τ; Table 2) by a factor of 2.7 (Table 4). The DO at the SWI is higher as Re_b is increased and the turbulent transport on the water side becomes more intense, in agreement with the observations of *Bryant et al.* [2010]. As Re_b increases the DO flux to the sediment, across the SWI, increases due to the thinning of the diffusive sublayer and the resulting higher oxygen uptake by the sediment layer can only be sustained by higher DO concentration at the SWI and higher penetration depth. However, the mean DO response to Re_b increases becomes less pronounced at higher Re_b. This is consistent with classical results in heat and mass transfer [*Pinczewski and Sideman*, 1974; *Schwertfirm and Manhart*, 2007] where the gain in mass transfer rate across the interface, as mixing on the fluid side is enhanced, is reduced at higher Reynolds numbers. The limiting factor for the

Figure 8. Effect of Reynolds number: (a) Mean scalar profile, (b) RMS intensity and (c) total turbulent flux. LES-3 (high-Re) is the dash-dotted line, LES-3 is the solid line and LES-3 (low-Re) is the dashed line.
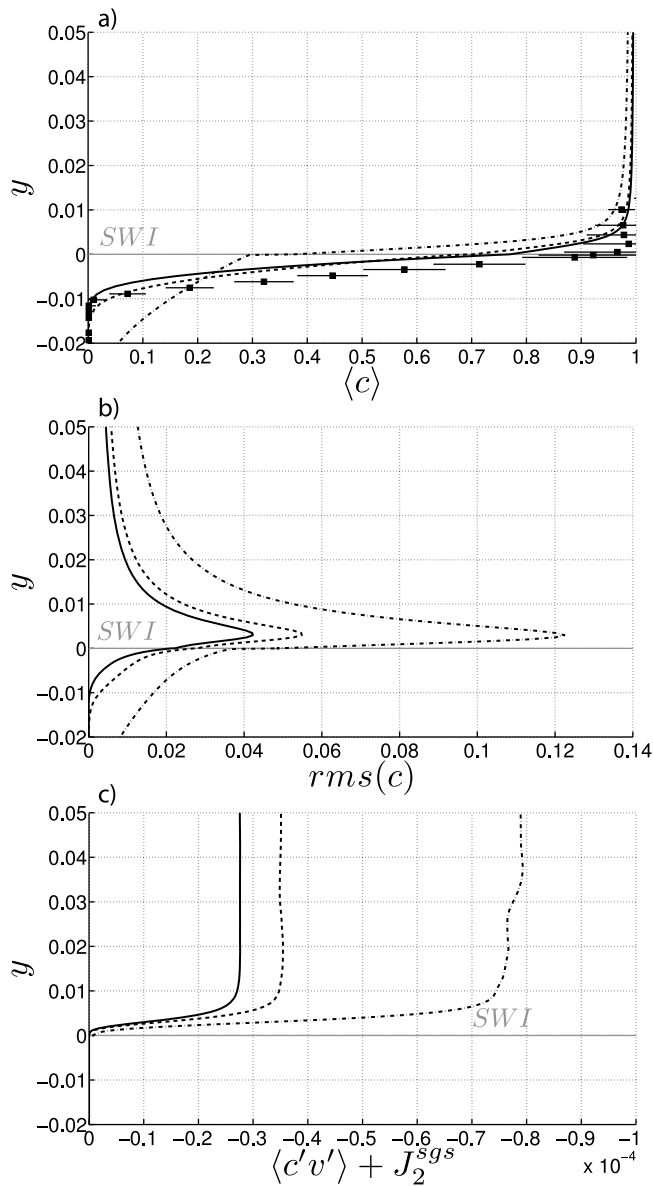
Figure 9. Effect of intrinsic permeability: (a) Mean scalar profile, (b) RMS intensity and (c) total turbulent flux. LES-4 is the solid line, LES-4 (K-6) is the dashed line and LES-4 (K-5) is the dash-dotted line (respectively, $K^* = 0$, $K^* = 10^{-6}$ cm^2, $K^* = 10^{-5}$ cm^2).

sediment uptake lies in the nature of the fluid side transport, regardless of the presence of an underlying absorbing medium.

[40] We conclude that, overall, the model reacts as expected to changes in turbulent activity. The resolved scalar RMS peak approaches the SWI as the Reynolds number is increased (thinning of the diffusive sublayer is predicted by the model); the total value of the scalar turbulent flux (non-dimensionalized by $C_b U_b$) is reduced by the increased Reynolds number (reduced mean scalar gradient at the wall). This is understood by analyzing the dimensionless governing equations: as the reference current velocity U_b is increased the non-dimensional value of the DO utilization rate $\mu_\chi = \mu_\chi^* \nu / U_b^2$ is reduced. The SOD dimensional

counterpart (that can be obtained by multiplying the free-stream value of the total turbulent flux in Figure 8c by $C_b U_b$) does, however, increase as observed experimentally.

3.6. Effects of Pore Water Flow Induced Transport

[41] To this point the effects of pore water induced solute transport in the sediment layer—advection and dispersion—have not been considered (i.e., the results shown have been for $K^* = 0$). *Higashino et al.* [2008], who modeled the turbulent transport with an algebraic RANS model in a developing flat plate boundary layer, also observed disagreement between their model and the experimental data for the higher Reynolds number cases. They argued that the reason for such discrepancies is that the permeability of the sediment layer was not fully taken into account. Velocity fluctuations are expected to penetrate in the sediments extending the turbulence-driven transport to this layer. Moreover, the newly introduced advective flux should increase the value of the oxygen concentration at the SWI. Subsequent investigations by the same author showed no improvement for small K^*, worsening of the agreement for higher K^* as anticipated in the Introduction.

[42] To shed some light on these issues we have investigated the effects of advection and dispersion—both processes governed by the permeability—in the sediment for case LES-4. Figure 9 shows the effects of non-zero permeability on the DO distribution. Values of intrinsic permeability up to $K^* = 10^{-6}$ cm^2 ($K^* = 0$ corresponding to no pore water flow in the sediment layer) do not affect the mean DO distribution significantly. If the permeability is furthermore increased to $K^* = 10^{-5}$ cm^2 the effective diffusivity in the sediment layer increases dramatically, increasing the SOD and, consequently, the flux on the water-side. This leads to rather low values of oxygen concentration at the interface that are not consistent with the experimental observations at higher Reynolds numbers and is similar to what was observed by *Higashino and Stefan* [2011]. Moreover, typical values of permeability for sediments of the type used in the experiments are between one and two orders of magnitude lower than this value [*Boudreau and Jørgensen*, 2001; *Huettel and Gust*, 1992; *Wiebke Ziebis and Forster*, 1996].

[43] In Figure 10 we show the RMS velocity fluctuations and the DO fluxes on the sediment side for runs LES-4 (K-6) and LES-4 (K-5). All of these quantities are maximum at the SWI where the direct forcing by the turbulent pressure waves from the water side takes place. The values of velocity RMS are negligible with respect to the corresponding water side quantities. The correlation between fluctuations of the vertical component of the interstitial velocity and scalar fluctuations (not available in a RANS code) in the sediment layer creates an advective flux (mean advection is zero in the porous medium), shown in Figure 10b (amplified by a factor of 100). Its value is negligible with respect to the diffusive and dispersive fluxes (between 2 or 3 orders of magnitude lower). Since the magnitude of the effective diffusivity directly depends on the intensity of the pore water flow based on (10) the model yields a strong discontinuity in the DO total diffusivity across the SWI, from purely molecular to fully dispersive, that is evident in Figure 9a.

[44] The pressure is continuous across the SWI, as shown in Figure 11a. The interstitial flow in the sediment layer is
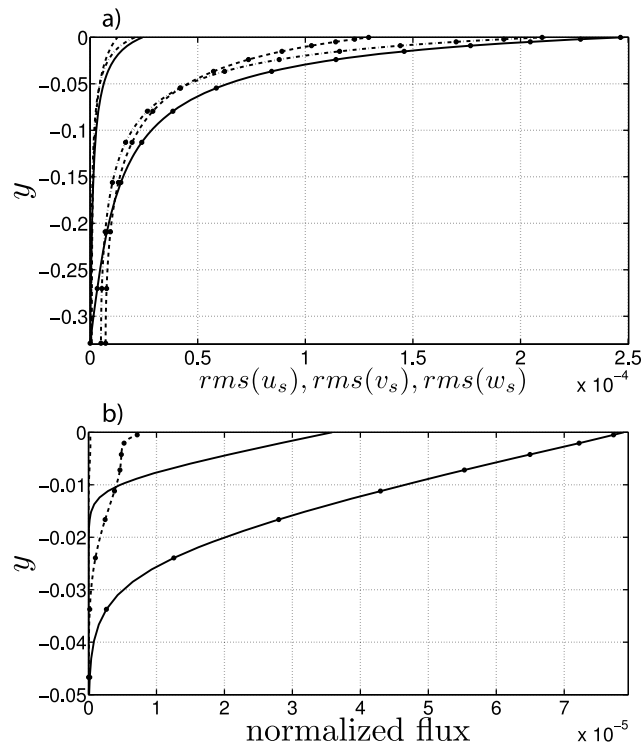
Figure 10. Fluid statistics in the sediment layer for calculations including the pore water flow for LES-4 (K-6) and LES-4 (K-5) runs shown without and with circle markers, respectively. (a) RMS velocity fluctuations; v_{rms} is the solid line, u_{rms} is the dashed line and w_{rms} is the dash-dotted line. (b) Comparison between total diffusive and dispersive flux (solid line) and advective flux (amplified by $\times 100$) in the sediment layer (dashed line).

driven from high pressure to low pressure regions; however, its intensity is too low (of the order of $10^{-5} U_b$ for the run LES-4 (K-6)) to significantly affect the net mass transfer rate across the interface. The corresponding DO concentration contours in Figure 11b are consistent with the near-wall high-Schmidt-number transport dynamics described by *Pinczewski and Sideman* [1974]: regions of above-average pressure at the wall, like the ones at $x = 1.1$ (bursting events), are caused by eddies, rich in oxygen, that are strong enough to reach the SWI, and that, only after some time, cause the thinning of the diffusive sublayer (enhancing the instantaneous mass transfer rate across the SWI). The existence of such time lag (due to diffusive transport times) explains why in Figure 11 a patch of high pressure, traveling in the direction of the mean current at approximately the friction velocity, is leading an elongated streak (from $x = 0$ to $x = 1.1$) of higher-than-average mass flux at the SWI, also visible in Figure 4a; since both pressure and DO concentration fields are advected downstream, the time lag between the occurrences of these two events determines the observed shift in space, which is a function of the Schmidt and Reynolds numbers.

[45] The DO penetration depth in the sediment layer and DO concentration at the SWI, are not immediately affected by instantaneous variations in water-side transport dynamics. This is due to the long diffusive timescales, associated with the transport in the porous medium and across the diffusive sublayer, compared to the ones characterizing the turbulent transport above it. The ratio of the two timescales is proportional to $Sc^{-1/3}$. This determines a time lag between the sequence of small-scale transport processes (water-side turbulent transport, transfer across the SWI and transport in the porous medium) that ultimately leads to DO consumption in
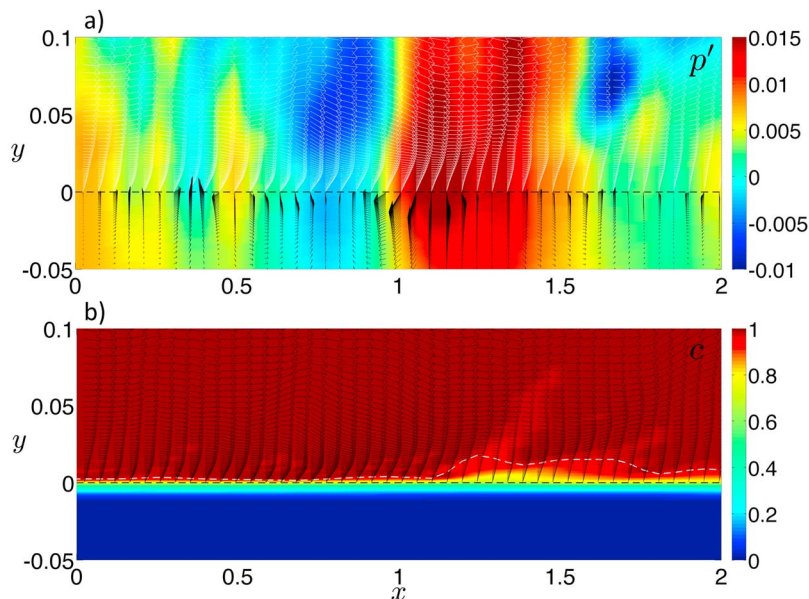
Figure 11. Contours of (a) instantaneous pressure and (b) DO concentration with (estimated) thickness of the diffusive sublayer (white dashed line) in the $z = 0.57$ plane with velocity vector plot (velocity vectors in sediments are amplified by $\times 1000$ for clarity) for case LES-4 (K-6) at $K^* = 10^{-6}$ cm^2 ($K = 1.7 \times 10^{-8}$). Note that the pressure field is scaled with $\rho U_b^2 = 6.9$ Pa, the oxygen concentration field with $C_b = 4.5$ mg l^{-1} and the coordinates x, y with $\delta = 7.6$ cm.

the sediment layer. The sediment layer retains the signature of the overlying turbulent transport events.

3.7. Effect of Duct Geometry

[46] Another potential reason for the disagreement between the model and the experiments is the effect of the duct geometry. The experiments were carried out in a square duct, our calculations in a plane channel. We have also performed simulations of the flow field only in a square duct, for $Re_{max} = 3000$ and 4600 and compared them with the channel flow calculations (at the same Reynolds numbers). We notice that in every case (and, more remarkably, in the higher Reynolds number case) the channel flow exhibits a more extended turbulent mixed region, than the one present in the symmetry plane of a square duct, indicative of more efficient local transport of momentum from the centerline toward the wall for the channel flow. LES of cases EXP-4 and EXP-5, performed in a square duct configuration, would therefore cause the numerical predictions to either remain unchanged, or further deviate from the observations (which exhibit a more extended region of turbulent mixed DO concentration than the simulations). We therefore conclude that the cause for observed disagreement for the higher Reynolds number cases should not be sought in the geometry of the flow duct.

4. Conclusions

[47] We developed a model for dissolved oxygen (DO) transfer, from water to underlying organic sediment beds that, for the first time, couples large-eddy simulation (LES) of turbulent transport on the water side with existing biogeochemical models for the transport and the DO bacterial absorption in the sediment bed. As opposed to a RANS model, LES provides unsteady and time-resolved data allowing us to visualize and analyze instantaneous events in the flow, such as bursts. This allows us to determine the role of turbulent coherent structures in controlling the diffusive sublayer thickness and, thus, sustaining the mass transfer rate across the SWI, or, equivalently, the sediment oxygen demand (SOD). Differences between the characteristic timescales of the transport in the sediment layer, with respect to the overlying turbulent flow, are also quantified. Instantaneous visualizations of the velocity and concentration fluctuations reveal a flow pattern organization (determined by near-wall coherent motions) that is still retained at the SWI and leaves its signature within the sediment layer. Relying on an accurate description of the flow, on the water-side, has also the advantage of better describing turbulence-driven transport processes in the sediment layer, improving, therefore, the prediction of the SOD. These include pore water-flow driven advection and dispersion, which directly depend on the instantaneous pressure distribution at the sediment-water interface (SWI), not available in a RANS code.

[48] The computational tool presented here can be applied to investigate the modeling issues of near-wall oxygen depletion and transfer dynamics in water-bodies. Very good agreement is found with experiments at low and intermediate Reynolds numbers (cases EXP-2 and EXP-3). For higher Re_b the agreement between experiments and simulations is recovered by applying a vertical shift to the data of 0.23 and 0.11 mm for cases EXP-4 and EXP-5, respectively. A sensitivity analysis, to all of the important material properties (including bacterial population, current intensity, permeability), has been carried out to try to explain such discrepancies and, at the same time, to estimate the relative importance of the different physical processes involved in the problem. The SOD response to changes in bacterial population is almost linear, whereas increases in the current intensity reveal slow gains in the overall DO depletion rate, despite the presence of an absorbing sediment layer. Transport dynamics on the water side are consistent with classic heat-and-mass transfer laws. Investigating the effects of a variable intrinsic permeability $K*$ has revealed that mean pore water flow advection in the sediment layer, for the smooth organic sediments investigated here (clayey sand), is not an important process; dispersion, on the other hand, becomes important for permeabilities of $K* \geq 10^{-5}$ cm^2 which leads to oxygen distributions that appear unrealistic for our case.

[49] Future research, at lab scale, should focus on higher Reynolds numbers ($Re_{max} > 7000$) where numerical predictions are not consistent with experimental observations. Application of a fully coupled numerical and mathematical model to represent experiments like the ones presented here, requires, among other things, accurate measurements of porosity (or, mean profiles slope discontinuity at the SWI) and permeability, the most critical sediment layer material properties determining the mean oxygen distribution. Values of $\chi*$ are currently an output of calibration procedures performed with models like ours and are not easily determined a priori. Higher-order statistics (scalar variance and turbulent flux profiles) have to be measured and compared to companion numerical predictions; particular attention must be taken in order to avoid sediment resuspension or pre-resuspension phenomena that would lead to bi-phasic flow that is too difficult to account for in the model; at least at this stage of development. Additional experiments with permeable sands and carefully measured pore water-flow intensities would help understand the limits of applicability of the currently adopted numerical approach. Also, a special effort should be made by experimentalists who wish to collaborate with computational modelers in trying to adopt geometries amenable to LES and DNS studies, such as high-aspect-ratio ducts (well-approximated by a doubly periodic channel flow). All of the aforementioned suggestions can facilitate a synergistic interaction between experimental and numerical investigations. The goal is to avoid potential sources of disagreement between the two approaches, contaminating the analysis of the problem, which is already sufficiently complicated by a broad spectrum of physical processes. This joint effort is required to develop accurate numerical models for oxygen transport that can be adopted to calibrate RANS models for field scale applications such as water-quality management. An eddy-resolving model like LES is the ideal candidate for this task, as it can provide sufficient detail to carry out in-depth analysis of the governing mechanisms for oxygen transport and depletion at reasonable computational costs.

[50] The thus-obtained numerical model for oxygen transport could be easily extended to multiple species and contaminants transported in the fluid and in the porous medium, by taking into account, for example, the complete
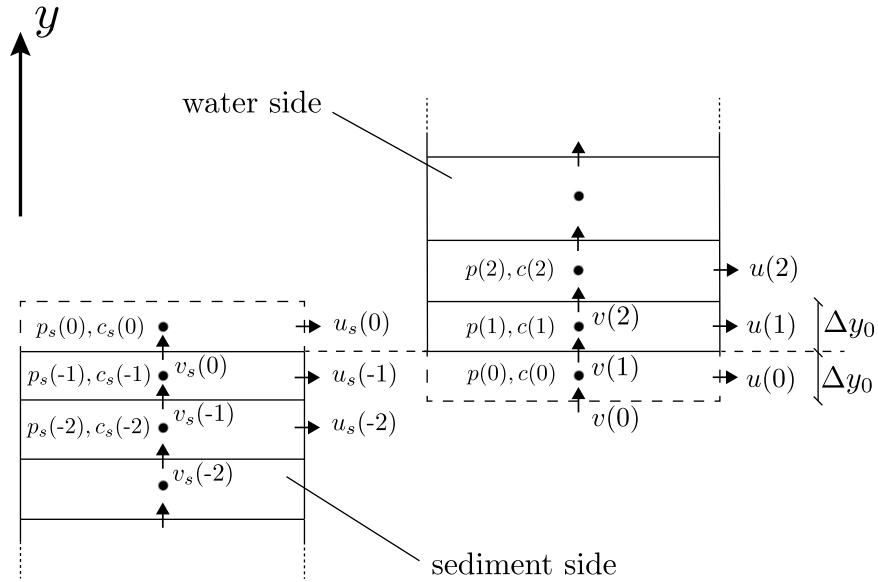
Figure A1. Schematic of the discretization used for the numerical setup of the implicit-two-layer coupling at sediment-water interface.

sediment biogeochemistry. This extension, although rather straightforward, would significantly broaden the scope of the developed model to problems where more accurate biochemical descriptions are required. The development and validation of the current numerical setup is a crucial step toward the design of accurately time-resolving transport models for solute exchange across the interface between fluid and porous media.

Appendix A: Numerical Modeling for Solute and Momentum Exchange Across the Sediment-Water Interface

[51] The coupling across the sediment-water interface of the two distinct sets of governing equations for the momentum and solute transport - one for the water-side (1), (2), (6) and the other for the sediment-side transport (8), (12) and (15)—can pose some implementation challenges. In order to numerically enforce the continuity of the solute concentration and momentum field (and their respective fluxes) across the SWI a 1D strategy for the coupling (only along y) has been adopted. This choice is due to the fact that the mass and momentum transport (if present) can occur only across the SWI via the wall-normal component of the respective fluxes. The details of the coupling procedure are described in the following with reference to Figure A1.

[52] Let Δt be the time step of the time advancement scheme. The update of the solution in the two layers from time n to time $n + 1$, is carried out via an implicit coupling across the SWI. The instantaneous velocity and oxygen distributions in the two layers are known at time n, i.e., c^n, v^n on the water side and c_s^n, v_s^n on the sediment side. The coupling is performed through the following steps:

[53] 1. A prediction of the oxygen concentration at the SWI for time $n + 1$ is obtained by an explicit update taking into account only the wall-normal components of the total flux; the solution is updated at the closest node to the SWI on the water side (indexes are with references to the figure)

$$
\begin{aligned}
\bar{c}^*(+1) = \bar{c}^n(+1) &+ \Delta t \frac{1}{Sc\,Re} \left.\widehat{\frac{\partial^2 \bar{c}}{\partial y^2}}\right|_{+1} \\
&- \frac{\Delta t}{\Delta y}\left[\bar{v}^n(+1)\left(\frac{\bar{c}^n(+2) + \bar{c}^n(+1)}{2}\right)\right. \\
&\left.- \bar{v}^n(0)\left(\frac{\bar{c}^n(+1) + \bar{c}^n(0)}{2}\right)\right]
\end{aligned}
\tag{A1}
$$

and sediment side

$$
\begin{aligned}
c_s^*(-1) = c_s^n(-1) &+ \Delta t \frac{1}{Sc_s Re} \left.\widehat{\frac{\partial^2 c_s}{\partial y^2}}\right|_{-1} \\
&- \frac{\Delta t}{\Delta y}\left[-v_s^n(-1)\left(\frac{c_s^n(-2) + c_s^n(-1)}{2}\right)\right. \\
&\left.+ v_s^n(0)\left(\frac{c_s^n(0) + c_s^n(-1)}{2}\right)\right],
\end{aligned}
\tag{A2}
$$

where $\left.\widehat{\partial^2 \bar{c}/\partial y^2}\right|_{+1}$ is a numerical estimate of $\widehat{\partial^2 \bar{c}/\partial y^2}$ at $y = +\Delta y_0/2$, linearly dependent on $\bar{c}^n(0)$, $\bar{c}^n(+1)$ and $\bar{c}^n(+2)$; likewise, $\left.\widehat{\partial^2 \bar{c}/\partial y^2}\right|_{-1}$ is a numerical estimate of $\widehat{\partial^2 c_s/\partial y^2}$ at $y = -\Delta y_0/2$, linearly dependent on $c_s^n(0)$, $c_s^n(-1)$ and $c_s^n(-2)$. The final prediction is obtained by averaging the two values above thus yielding

$$
c_{swi}^* = \frac{1}{2}\left[\bar{c}^*(1) + c_s^*(-1)\right].
\tag{A3}
$$

[54] 2. The value of c_{swi}^* is applied as a Dirichlet boundary condition at time $n + 1$ to implicitly update the solution in the sediment layer.

[55] 3. An implicit update of the oxygen distribution on the water side is now possible by prescribing the DO flux at time $n + 1$ (extracted from the updated c_s field)

$$\frac{1}{Sc\,Re_b}\frac{\bar{c}^{n+1}(1) - \bar{c}^{n+1}(0)}{\Delta y_0} = \frac{1}{Sc_s Re_b}\frac{c_s^{n+1}(0) - c_s^{n+1}(-1)}{\Delta y_0} \quad (A4)$$

(the scalar convective flux is treated explicitly everywhere, implicit update is just applied to the diffusive fluxes).

[56] 4. The velocity field is updated; therefore, the pressure distribution p^{n+1} is known in the channel.

[57] 5. The governing equations for the interstitial velocity field are directly solved given the fluid-side distribution of pressure fluctuations at the SWI. The boundary conditions for the Laplace equation

$$\widehat{\nabla^2} p_s^{n+1} = 0 \quad (A5)$$

are

$$\frac{p_s^{n+1}(0) + p_s^{n+1}(-1)}{2} = p^{n+1}(+1), \quad (A6)$$

$$\widehat{\frac{\partial p_s}{\partial y}} = 0 \quad at \quad y = -\delta_s/\delta. \quad (A7)$$

[58] 6. The boundary conditions for the velocity field at the next cycle on the water side are

$$v^{n+1}(0) = v_s^{n+1}(-1) = -K\,Re_b\frac{p_s^{n+1}(0) - p_s^{n+1}(-1)}{\Delta y_0}. \quad (A8)$$

The velocity in the channel is updated implicitly; this strategy introduces a time lag. The only additional numerical accuracy requirement of this scheme is that the grid spacing at the SWI, Δy_0, must be the same from both sides (see Figure A1).

References

Antonia, R., and P. Orlandi (2003), Effect of Schmidt number on small-scale passive scalar turbulence, *Appl. Mech. Rev.*, 56(6), 615–632.

Bear, J. (1972), *Dynamics of Fluid in Porous Media*, Am. Elsevier, New York.

Bedford, K., and M. Abdelrhman (1987), Analytical and experimental studies of the benthic boundary layer and their applicability to near-bottom transport in Lake Erie, *J. Great Lakes Res.*, 13(4), 628–648.

Bergant, R., and I. Tiselj (2007), Near-wall passive scalar transport at high Prandtl numbers, *Phys. Fluids*, 19, 065105.

Boegman, L., M. R. Loewen, D. A. Culver, P. F. Hamblin, and M. N. Charlton (2008a), Spatial-dynamic modeling of algal biomass in Lake Erie: Relative impacts of dreissenid mussels and nutrient loads, *J. Environ. Eng.*, 134(6), 456–468.

Boegman, L., M. Loewen, P. Hamblin, and D. Culver (2008b), Vertical mixing and weak stratification over zebra mussel colonies in western Lake Erie, *Limnol. Oceanogr.*, 53(3), 1093–1110.

Boegman, L., and G. N. Ivey (2009), Flow separation and resuspension beneath shoaling nonlinear internal waves, *J. Geophys. Res.*, 114, C02018, doi:10.1029/2007JC004411.

Boudreau, B. (1996), The diffusive tortuosity of fine-grained unlithified sediments, *Geochim. Cosmochim. Acta*, 60(16), 3139–3142.

Boudreau, B., and B. Jørgensen (2001), *The Benthic Boundary Layer: Transport Processes and Biogeochemistry*, Oxford Univ. Press, New York.

Bouldin, D. (1968), Models for describing the diffusion of oxygen and other mobile constituents across the mud-water interface, *J. Ecol.*, 56(1), 77–87.

Bryant, L. D., C. Lorrai, D. F. McGinnis, A. Brand, A. Wüest, and J. C. Little (2010), Variable sediment oxygen uptake in response to dynamic forcing, *Limnol. Oceanogr.*, 55(2), 950–964.

Calmet, I., and J. Magnaudet (1997), Large-eddy simulation of high-Schmidt-number mass transfer in a turbulent channel flow, *Phys. Fluids*, 9, 438–456.

Chriss, T., and D. Caldwell (1982), Evidence for the influence of form drag on bottom boundary layer flow, *J. Geophys. Res.*, 87(C6), 4148–4154.

Dade, W. (1993), Near-bed turbulence and hydrodynamic control of diffusional mass transfer at the sea floor, *Limnol. Oceanogr.*, 38(1), 52–69.

Diaz, R., and R. Rosenberg (2008), Spreading dead zones and consequences for marine ecosystems, *Science*, 321(5891), 926–929.

Dong, Y., X. Lu, and L. Zhuang (2003), Large eddy simulation of turbulent channel flow with mass transfer at high-Schmidt numbers, *Int. J. Heat Mass. Transfer*, 46(9), 1529–1539.

Freeze, R., and J. A. Cherry (1979), *Groundwater*, Prentice Hall, Englewood Cliffs, N. J.

Germano, M., U. Piomelli, P. Moin, and W. Cabot (1991), A dynamic sub-grid-scale eddy viscosity model, *Phys. Fluids A*, 3, 1760–1765.

Hendry, R., and C. Wunsch (1973), High Reynolds number flow past an equatorial island, *J. Fluid Mech.*, 58(01), 97–114.

Higashino, M., and H. Stefan (2011), Dissolved oxygen demand at the sediment-water interface of a stream: Near-bed turbulence and pore water flow effects, *J. Environ. Eng.*, 137(7), 531–541.

Higashino, M., C. J. Gantzer, and H. G. Stefan (2004), Unsteady diffusional mass transfer at the sediment/water interface: Theory and significance for SOD measurement, *Water Res.*, 38(1), 1–12.

Higashino, M., B. L. O'Connor, M. Hondzo, and H. G. Stefan (2008), Oxygen transfer from flowing water to microbes in an organic sediment bed, *Hydrobiologia*, 614(1), 219–231.

Higashino, M., J. Clark, and H. Stefan (2009), Pore water flow due to near-bed turbulence and associated solute transfer in a stream or lake sediment bed, *Water Resour. Res.*, 45, W12414, doi:10.1029/2008WR007374.

Hipsey, M., J. Romero, J. Antenucci, and D. Hamilton (2006), The Computational Aquatic Ecosystem Dynamics Model (CAEDYM): v3.1, report, Cent. for Water Res., Perth, West. Aust., Australia.

Hondzo, M., T. Feyaerts, R. Donovan, and B. O'Connor (2005), Universal scaling of dissolved oxygen distribution at the sediment-water interface: A power law, *Limnol. Oceanogr.*, 50(5), 1667–1676.

Huettel, M., and G. Gust (1992), Solute release mechanisms from confined sediment cores in stirred benthic chambers and flume flows, *Mar. Ecol. Prog. Ser.*, 82(2), 187–197.

Iversen, N., and B. Jørgensen (1993), Diffusion coefficients of sulfate and methane in marine sediments: Influence of porosity, *Geochim. Cosmochim. Acta*, 57(3), 571–578.

Keating, A., U. Piomelli, K. Bremhorst, and S. Nešić (2004), Large-eddy simulation of heat transfer downstream of a backward-facing step, *J. Turbulence*, 5(20), 1–27.

Koseff, J., J. Holen, S. Monismith, and J. Cloern (1993), Coupled effects of vertical mixing and benthic grazing on phytoplankton populations in shallow, turbid estuaries, *J. Mar. Res.*, 51(4), 843–868.

Leon, L. F., R. E. Smith, M. R. Hipsey, S. A. Bocaniov, S. N. Higgins, R. E. Hecky, J. P. Antenucci, J. A. Imberger, and S. J. Guildford (2011), Application of a 3D hydrodynamic-biological model for seasonal and spatial dynamics of water quality and phytoplankton in Lake Erie, *J. Great Lakes Res.*, 37(1), 41–53.

Leonard, A. (1974), Energy cascade in large-eddy simulations of turbulent fluid flows, *Adv. Geophys.*, 18, 237–248.

Lilly, D. K. (1992), A proposed modification of the germano subgrid-scale closure method, *Phys. Fluids A*, 4, 633–635.

Lorke, A., B. Müller, M. Maerki, and A. Wüest (2003), Breathing sediments: The control of diffusive transport across the sediment-water interface by periodic boundary-layer turbulence, *Limnol. Oceanogr.*, 48(6), 2077–2085.

Lorrai, C., D. McGinnis, P. Berg, A. Brand, and A. Wüest (2010), Application of oxygen eddy correlation in aquatic systems, *J. Atmos. Oceanic Technol.*, 27, 1533–1546.

Moser, R., J. Kim, and N. Mansour (1999), Direct numerical simulation of turbulent channel flow up to Re = 590, *Phys. Fluids*, 11, 943–946.

Na, Y. (2004), On the large-eddy simulation of high-Prandtl-number scalar transport using dynamic subgrid-scale model, *J. Mech. Sci. Technol.*, *18*(1), 173–182.

O'Connor, B. L., and J. Harvey (2008), Scaling hyporheic exchange and its influence on biogeochemical reactions in aquatic ecosystems, *Water Resour. Res.*, *44*, W12423, doi:10.1029/2008WR007160.

O'Connor, B. L., and M. Hondzo (2007), Enhancement and inhibition of denitrification by fluid-flow and dissolved oxygen flux to stream sediments, *Environ. Sci. Technol.*, *42*(1), 119–125.

O'Connor, B. L., and M. Hondzo (2008), Dissolved oxygen transfer to sediments by sweep and eject motions in aquatic environments, *Limnol. Oceanogr.*, *53*(2), 566–578.

Patterson, J. C., B. R. Allanson, and G. N. Ivey (1985), A dissolved oxygen budget model for Lake Erie in summer, *Freshwater Biol.*, *15*(6), 683–694, doi:10.1111/j.1365-2427.1985.tb00242.x.

Pinczewski, W., and S. Sideman (1974), A model for mass (heat) transfer in turbulent tube flow. Moderate and high Schmidt (Prandtl) numbers, *Chem. Eng. Sci.*, *29*(9), 1969–1976.

Quaresma, L., J. Vitorino, A. Oliveira, and J. da Silva (2007), Evidence of sediment resuspension by nonlinear internal waves on the western Portuguese mid-shelf, *Mar. Geol.*, *246*(2–4), 123–143.

Rabalais, N., R. Diaz, L. Levin, R. Turner, D. Gilbert, and J. Zhang (2010), Dynamics and distribution of natural and human-caused hypoxia, *Biogeosciences*, *7*(2), 585–619.

Røy, H., M. Huettel, and B. B. Joergensen (2004), Transmission of oxygen concentration fluctuations through the diffusive boundary layer overlying aquatic sediments, *Limnol. Oceanogr.*, *49*(3), 686–692.

Sanford, T., and R. Lien (1999), Turbulent properties in a homogeneous tidal bottom boundary layer, *J. Geophys. Res.*, *104*(C1), 1245–1257.

Schwertfirm, F., and M. Manhart (2007), DNS of passive scalar transport in turbulent channel flow at high Schmidt numbers, *Int. J. Heat Fluid Flow*, *28*(6), 1204–1214.

Trolle, D., H. Skovgaard, and E. Jeppesen (2008), The water framework directive: Setting the phosphorus loading target for a deep lake in Denmark using the 1D lake ecosystem model DYRESM-CAEDYM, *Ecol. Modell.*, *219*(1–2), 138–152.

Veenstra, J., and S. Nolen (1991), In-situ sediment oxygen demand in five Southwestern U.S. lakes, *Water Res.*, *25*(3), 351–354.

Wiebke Ziebis, M., and S. Forster (1996), Impact of biogenic sediment topography on oxygen fluxes in permeable seabeds, *Mar. Ecol. Prog. Ser.*, *140*, 227–237.

Zang, Y., R. Street, and J. Koseff (1993), A dynamic mixed subgrid-scale model and its application to turbulent recirculating flows, *Phys. Fluids A*, *5*, 3186–3197.